IoT-Inspired Cooperative Spectrum Sharing with Energy Harvesting in UAV-Assisted NOMA Networks: Deep Learning Assessment

Ratnesh Kumar, *Student Member, IEEE*, Chandan Kumar Singh, *Student Member, IEEE*,
Prabhat Kumar Upadhyay, *Senior Member, IEEE*, Anas M. Salhab, *Senior Member, IEEE*,
Ali Arshad Nasir, *Member, IEEE*, and Mudassir Masood Ali, *Member, IEEE*

Abstract—Energy and spectral efficiency of Internet of Things (IoT) networks can be improved by integrating energy harvesting, cognitive radio, and non-orthogonal multiple access (NOMA) techniques, while unmanned aerial vehicles (UAVs), on the other hand, are a quick and adaptable entity for improving the coverage performance. In this article, we assess the performance of a UAV-assisted overlay cognitive NOMA (OC-NOMA) system by employing an energy harvesting based IoT-inspired cooperative spectrum sharing transmission (I-CSST) scheme. Herein, an energy-constrained UAV-borne secondary node harvests radio-frequency energy from the primary source and uses it to send both its own information signal and the primary information signal using the NOMA approach. We consider the impact of the imperfect successive interference cancellation in NOMA and the distortion noises caused by hardware impairments (HIs) in signal processing, which are unavoidable in real-world systems. We obtain the complicated expressions of outage probability (OP) for primary and secondary IoT networks using I-CSST scheme under heterogeneous Rician and Nakagami-*m* fading channels. We continue to investigate asymptotic analysis for OP in order to gain insightful knowledge on the high signal-to-noise ratio (SNR) slope and practicable diversity order. We also assess the system throughput and energy efficiency for the considered OC-NOMA system. Our results demonstrate the benefits of the suggested I-CSST scheme over the benchmark primary direct transmission and orthogonal multiple access schemes. We create a deep neural network (DNN) architecture for real-time OP prediction in order to combat the complications in model-based approaches.

Index Terms—Cognitive radio, deep neural network, energy harvesting, hardware impairments, non-orthogonal multiple access, overlay spectrum sharing system, unmanned aerial vehicle.

I. INTRODUCTION

THE increasing amount of mobile data traffic motivates researchers to look into spectral-efficient and energy-efficient communication strategies in sixth-generation (6G)

wireless networks [1]. In order to meet customer demands in the near future, the limited amount of spectrum that is now accessible must be used effectively [2]. The need for high data transfer speeds, improvements in quality of service (QoS), connecting massive equipment, etc., has aggravated this situation. Beyond spectral efficiency, energy efficiency has also emerged as a crucial issue for designing future Internet of Things (IoT) networks [3], [4]. When the devices are distantly located and lack a regular power source, energy consumption becomes more of an issue. The simultaneous wireless information and power transfer (SWIPT) technology, which enables wireless devices to simultaneously process information and harvest energy from ambient radio-frequency (RF) signals, can solve such issues [5]. For SWIPT realization, there are two prevalent schemes: time switching (TS) and power splitting (PS) [6] . In PS-based SWIPT, a part of the received power is used for energy harvesting (EH) and the remaining amount for the information processing (IP) operation, while in TS-based SWIPT, time is alternated between the EH and IP phases [7].

A. Background Works

A promising method to control the rapidly expanding number of mobile applications over the finite spectrum is cognitive radio (CR) [8]. It can significantly increase the spectral efficiency of wireless networks using the interweave, underlay, and overlay paradigms of spectrum access. Both the underlay and overlay models permit simultaneous data transmissions of primary users (PUs) and secondary users (SUs) over the same frequency band, provided that the QoS constraint for the PU is met, unlike the interweave model, which depends on spectrum sensing and opportunistic spectrum access. If the interference constraint at the PU is satisfied, the SU can transmit data using an underlay technique [9] in the direction of its destination. In contrast, in an overlay model, SU prioritizes helping the PU's communication through relay cooperation in exchange for access to the PU's licensed spectrum [10], [11]. Non-orthogonal multiple access (NOMA) allows numerous users to get multiplexed in the power domain and send over the same time/frequency band, in contrast to orthogonal multiple access (OMA). To do this, it uses successive interference cancellation (SIC), which demultiplexes the superimposed signals at the receiver, in conjunction with superposition coding at the transmitter [12]. Eventually, the cognitive NOMA approach,

which integrates NOMA with CR, has shown to be a potential method for improving spectral efficiency in future wireless networks [13]. In this sense, several studies have examined cognitive NOMA systems utilising both the underlay [14], [15] and overlay [17], [18] models. The authors investigated NOMA for the large-scale underlay CR networks in [14], and used a stochastic geometry approach to examine the outage probability (OP) performance. Furthermore, a decode-and-forward (DF) [15] relaying protocol was used to assess the OP measure of SUs in underlay cognitive NOMA relay networks. An overlay model uses the secondary transmitter (ST) as a relay for PU and also enables it to communicate with the secondary receivers (SRs) by implementing the NOMA principle, in contrast to the underlay cognitive NOMA model [16], [17]. In [18], an overlay NOMA spectrum sharing approach was used to serve numerous PUs over an integrated satellite-terrestrial network. It should be highlighted that the overlay NOMA model might eliminate the interference temperature constraint from the ST to the primary receiver (PR), and thereby, it can improve the OP performance of the PU through ST (relay) as a means of cooperative diversity advantage.

Deploying EH in CR networks is a promising development aiming to increase energy and spectral efficiency. Energy-limited SUs will be more able to sustain themselves since they can share the spectrum and gather energy from nearby RF sources. Several studies have used SWIPT in cognitive NOMA systems [19]-[24]. Authors in [19] specifically proposed a novel cooperative multiple-input single-output SWIPT NOMA protocol, where a strong NOMA user serves as an EH relay and aids a weak NOMA user by adopting a PS scheme. The research in [20] examined a secondary network's secure energy efficiency maximization problem while also examining an underlay cognitive NOMA system. Authors in [21] focussed on power beacon (PB)-assisted wireless-powered NOMA IoT systems. They demonstrated that the PB-assisted NOMA IoT system outperforms SWIPT NOMA system under a time switching mechanism based on an IoT relay. Authors of [22] investigated a CR system where the ST uses the RF signal from the primary transmitter (PT) to harvest the energy. The ST sends its data utilizing downlink NOMA and serves as the primary system's DF relaying service. The outage performance of cooperative CR networks with SWIPT was examined in [23], where the cognitive relay harvests the transmission power from the ST using the PS scheme, and the NOMA protocol uses the fixed power allocation scheme. In some additional studies, a full-duplex ST was chosen to convey the PT information for IoT network across a cooperative overlay spectrum sharing network, in return for which SUs might gather energy and investigate a chance of spectrum access [24].

Recent research has shown that deep learning (DL) approaches are useful for addressing a number of real-world problems in today's wireless communication networks, including resource allocation, congestion control, and queue management [25]. In order to increase a cell-edge user's productivity under both perfect SIC (pSIC) and imperfect SIC (iSIC), a deep neural network (DNN) was used in [26] for wireless powered CR-NOMA-based IoT relay networks. In [27], DNN was built to solve classification and regression problems in

cognitive two way relaying networks for relay selection. In [28], authors have examined a DNN integrated into a NOMA system, and demonstrated its remarkable performance in terms of channel encoding, decoding, and detection. Authors in [29] have presented a novel approach to optimizing service distribution in IoT networks, which uses deep learning to learn the optimal distribution strategy.

B. Motivation and Contributions

All the aforementioned works hypothesized the need for pSIC and ideal hardware at the RF transceivers to investigate the performance of SWIPT-enabled cognitive NOMA networks. Practical implementation of the pSIC is challenging. Additionally, due to amplifier non-linearities, in-quadrature-phase imbalances, and phase noises, RF transceivers are affected by hardware impairments (HIs) [30]-[33]. Future IoT networks are predicted to have a great number of inter-connections, so it would be necessary to include affordable devices to reduce the implementation cost. Such inexpensive equipment causes HIs. Even though different compensation algorithms could reduce the HIs, there are always some residual impairments in the real world. The SWIPT-based cognitive NOMA system may have capacity restrictions due to the impacts of iSIC and HIs, especially for high-rate applications. While several recent investigations [34], [35], and [36] have examined the effects of iSIC on the performance assessment of cognitive NOMA networks, but they have not considered potential SWIPT aspects. While a very recent work [37] has analyzed the OP performance of a cooperative NOMA-based IoT network with RF EH, but it has not considered the dynamic CR network which has a more richer functionality. To the best of authors' knowledge, no research has yet examined the performance analysis of cognitive NOMA systems inspired by SWIPT under the combined influences of HIs and iSIC. This analysis is crucial to understanding how iSIC and HIs will affect the practical design of cognitive NOMA IoT networks linked with the EH method for better sustainable communication in 6G environments.

Recently, unmanned aerial vehicles (UAVs) have become widely deployed as flying wireless access platforms for reliable communication. Recent advancements in drone technology have made it possible for wireless applications to create UAVs that are affordable, robust, and small. As a result, it is anticipated that UAV-assisted wireless communication will be a potential contender for IoT-inspired 6G networks [38]. For instance, considering both underwater and aerial segments, a UAV-assisted multi-access computation offloading using NOMA for marine communication networks was proposed in [39], with the objective of minimizing the energy consumption of ocean devices.

As a result of the previous discussion, we assess the performance of an EH-based overlay cognitive NOMA (OC-NOMA) system in this study by taking into account the impact of iSIC and HIs on the involved devices. SU node, which typically lacks a distinct spectrum for communication, could be the affordable energy-constrained components in small cell IoT networks. We specifically take into account a situation

of downlink communication between a PT and its PR with the assistance of a secondary network made up of a single ST-SR pair. In addition, ST is presumptively equipped with RF-based EH unit on a UAV, and it can serve as a DF relay for primary communications while using a shared spectrum for its own transmission. According to the NOMA principle, the ST divides its harvested power into two parts, relaying the primary signal and transmitting its own signal simultaneously. The following are the article's main contributions.

- We propose an EH-based IoT-inspired cooperative spectrum sharing transmission (I-CSST) scheme for the OC-NOMA system employing UAV-assisted DF relaying strategy. We also explore the primary direct transmission (PDT) scheme as a benchmark for evaluating the I-CSST's effectiveness for the OC-NOMA system under consideration. We further illustrate the relative performance advantages of I-CSST with NOMA compared to OMA.
- We thoroughly examine the accurate and asymptotic OP performance of the I-CSST schemes for primary and secondary IoT networks in the presence of HIs and iSIC over heterogeneous Rician and Nakagami-m fading environments based on the received signal-to-noise-and-distortion ratios (SNDRs) and signal-to-interference-noise-and-distortion ratios (SINDRs).
- With the help of the generated OP expressions, we provide a NOMA-based power allocation strategy, and evaluate the system throughput and energy efficiency to become aware of the OC-NOMA system.
- It is difficult to examine the OP for UAV-borne OC-NOMA systems because of their complex derivations. This creates a substantial hurdle for the model-based approach, therefore in order to achieve realistic real-time OCR-NOMA network setups, we construct a DNN model as an unique data-driven alternative for OP prediction with high accuracy and low latency. The execution time and root-mean-square error (RMSE) are the key metrics for evaluating the effectiveness and precision of our design method when predicting the performance of complicated network circumstances.

C. Paper Organization

The remainder of the paper is set up as follows. We analyze the I-CSST scheme and provide an illustration of the system and channel model in Section II. The primary network's OP performance analysis using the PDT and I-CSST schemes is presented in Section III. In Section IV, the secondary network's OP performance study is conducted. Section V assesses the system throughput and energy efficiency for the overall system. The DNN framework design is discussed in Section VI. The numerical and simulation findings are shown in Section VII, and conclusions are drawn in Section VIII. Additionally, the appendices provide the proof of useful theorems and lemmas.

Notations: A complex Gaussian distribution with a mean of zero and a variance of σ^2 is denoted as $\mathcal{CN}(0, \sigma^2)$. For a random variable X, the probability density function (PDF)
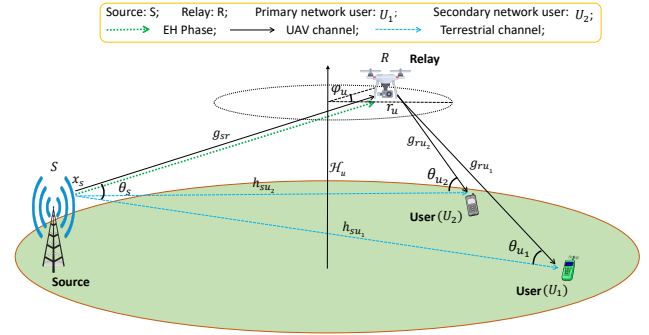

Fig. 1: OC-NOMA system model.

and cumulative distribution function (CDF) are denoted, respectively, by $f_X(\cdot)$ and $F_X(\cdot)$. Further, $\mathcal{K}_v(\cdot)$ is the modified Bessel function of the second kind as stated in [40, eq. 8.432.6], while $\Gamma(\cdot)$ and $\Upsilon(\cdot, \cdot)$ are the complete Gamma function and lower incomplete Gamma function, respectively, as stated in [40, eqs. (8.310.1) and (8.350.1)]. $\mathbb{E}[\cdot]$ stands for expectancy, and $\binom{p}{q} = \frac{p!}{q!(p-q)!}$ be the coefficient of the binomial.

II. SYSTEM MODEL AND I-CSST SCHEME DESCRIPTION

In this section, we describe the concerned OC-NOMA system and channel models, and explain the proposed EH-based I-CSST scheme using DF relaying strategy.

A. System and Channel Models

We consider an OC-NOMA system as shown in Fig. 1, which consists of a primary source (S), a secondary source (R) which also acts as a relay, and two users viz., a PU (U_1) and a SU (U_2). Herein, the primary source S transmits its message signal to the PU U_1 with the help of the relay R which is deployed over a UAV[1]. As such, we consider a UAV-assisted system where the UAV communicates with two NOMA users, i.e., U_1 and U_2. The UAV flies at an altitude of h, a constant velocity of v, and a circular trajectory of r. Even though main channel has been allotted between S and U_1, the S might still approach the adjacent R for assistance and harnessing a diversity advantage. In exchange, the R can use the primary's authorized spectrum for its own transmission to the SU U_2. The S is regarded as having a reliable power source feeding it, and broadcasts its signal at a constant transmit power. As the R being assumed as an energy-constrained node, it harvests energy from the RF signals transmitted by the primary source S. In anticipation of helping with the primary transmission between the S and U_1, the R is given access to the licensed primary spectrum based on an overlay paradigm. For this, R serves as a cooperative relay and uses the NOMA approach to concurrently transmit its own signal to the SU and help

---

[1]UAVs face several key challenges [41], including limited flight time and battery life, payload capacity restrictions, communication and control complexities, and the need for effective sense-and-avoid capabilities. To overcome these challenges [42], accounting for the weight of the UAV, air density, and rotor disc area is essential. These factors should be carefully considered in UAV design, analysis, and performance evaluations to ensure optimal performance and operational efficiency.

forward the primary source's signal to the PU. To examine the underlying I-CSST scheme for the OC-NOMA system under consideration, as explained in the sequel, we here utilize a PS-based EH technique.

The coordinates of ground nodes S, U_1, and U_2 in three-dimensional (3-D) Cartesian space are denoted by $\mathbf{v}_s = (\mathcal{X}_s, \mathcal{Y}_s, 0)$, $\mathbf{v}_{u_1} = (\mathcal{X}_{u_1}, \mathcal{Y}_{u_1}, 0)$, and $\mathbf{v}_{u_2} = (\mathcal{X}_{u_2}, \mathcal{Y}_{u_2}, 0)$, respectively. It is expected that the UAV will follow a circular trajectory with radius r_u, height $\mathcal{H}_u$ so that $\mathcal{H}_u \in [\mathcal{H}_u^{\min}, \mathcal{H}_u^{\max}]$, and constant speed, where $\mathcal{H}_u^{\min}$ and $\mathcal{H}_u^{\max}$ are the minimum and maximum allowed heights, respectively. Let φ_u represent the angle the UAV is presently positioned at with respect to the x-axis within the UAV circle. As a result, $\mathbf{v}_u = (r_u \cos \varphi_u, r_u \sin \varphi_u, \mathcal{H}_u)$ can be used to indicate the UAV's location. The locations of S, U_j, and the UAV can be denoted by the two-dimensional (2-D) Cartesian coordinates $\mathbf{w}_s = (\mathcal{X}_s, \mathcal{Y}_s)$, $\mathbf{w}_{u_j} = (\mathcal{X}_{u_j}, \mathcal{Y}_{u_j})$, and $\mathbf{w}_u = (r_u \cos \varphi_u, r_u \sin \varphi_u)$, respectively. Let $\theta_s = \arctan\left(\frac{\mathcal{H}_u}{|\mathbf{w}_u - \mathbf{w}_s|}\right)$ and $\theta_{u_j} = \arctan\left(\frac{\mathcal{H}_u}{|\mathbf{w}_u - \mathbf{w}_{u_j}|}\right)$, with $j \in \{1, 2\}$, provide the elevation angles (in rad) between S and the UAV and between users and the UAV, respectively.

We have assumed that all the nodes use single-antenna devices and operate in a half-duplex (HD) mode. Additionally, the devices have cheaper RF transceiver components installed, which accounts for their HIs. Since it is believed that every channel would adhere to the block fading, they will all stay the same for the duration of the block, but may vary on their own during the transmission over the different blocks. We have considered independent Nakagami-m fading [31] for the communication links from S to U_1 and U_2 with the channel coefficients h_{su_1} and h_{su_2}, respectively. The squared channel gain $|h_{ij}|^2$ follows the Gamma distribution with an average power of Ω_{ij} and a fading severity parameter of m_{ij}, for $i \in \{s\}$ and $j \in \{u_1, u_2\}$, with $i \neq j$. As a result, the corresponding PDF and CDF expressions of $|h_{ij}|^2$ can be obtained by

$$f_{|h_{ij}|^2}(z) = \frac{1}{\Gamma(m_{ij})} \left(\frac{m_{ij}}{\Omega_{ij}}\right)^{m_{ij}} (z)^{m_{ij}-1} e^{-\left(\frac{m_{ij}}{\Omega_{ij}}\right)z}, \quad (1)$$

and

$$F_{|h_{ij}|^2}(z) = \frac{1}{\Gamma(m_{ij})} \Upsilon\left(m_{ij}, \left(\frac{m_{ij}}{\Omega_{ij}}\right)z\right). \quad (2)$$

Once the path-loss model is taken into account, we obtain $\Omega_{ij} = d_{ij}^{-\alpha_{ij}}$, where d_{ij} is the normalised distance between nodes i and j and α_{ij} is the path-loss exponent. As a result, since the propagation energy decreases at the rate of $d_{ij}^{-\alpha_{ij}}$, the RF energy in the RF-based EH system could be harvested at very low power density. The additive white Gaussian noise (AWGN) with zero mean and variance σ^2 also has an impact on all receiving nodes.

In accordance with the elevation angle and surroundings, the communication links between the UAV and ground nodes (S, U_1, and U_2) may have line-of-sight (LoS) or non-LoS. As a result, the probability of LoS in their relevant links is provided by
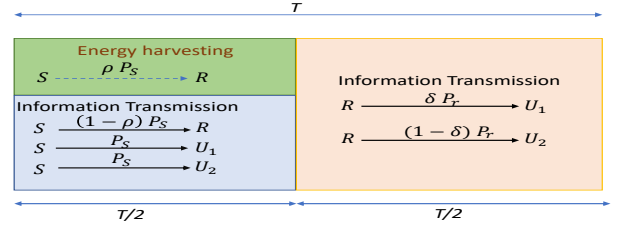

Fig. 2: Transmission block structure for the PS-based EH.

$$P_L(\theta_j) = \left(1 + \varepsilon_j \exp\left(-\xi_j(\theta_j - \varepsilon_j)\right)\right)^{-1}, \quad (3)$$

where ε_j and ξ_j, with $j \in \{s, u_1, \text{and } u_2\}$, denote the environment parameters fetched from the curve fitting using Damped Least-Squares (DLS) method [43]. The corresponding path-loss exponent is given by

$$\alpha_{r,j}(\theta_j) = P_L(\theta_j)\kappa_j + \nu_j, \quad (4)$$

where κ_j and ν_j, with ε_j and ξ_j, for $j \in \{s, u_1, \text{and } u_2\}$, represent constants that depend on the uplink and downlink environment [43]. The link between S and R is separated by $d_{sr} = \sqrt{|\mathbf{w}_u - \mathbf{w}_s|^2 + \mathcal{H}_u^2}$, and the link between R and U_k is separated by $d_{ru_k} = \sqrt{|\mathbf{w}_u - \mathbf{w}_{u_k}|^2 + \mathcal{H}_u^2}$. The related aerial path-loss exponents are $\alpha_{r,s}(\theta_s)$ and $\alpha_{r,u_k}(\theta_{u_k})$, respectively. Likewise, we assume that $d_{su_k} = |\mathbf{w}_s - \mathbf{w}_{u_k}|^2$ and α_{su_k}, where $k \in \{1, 2\}$, are the distance and path-loss exponent, respectively, for the corresponding terrestrial channel.

The channel between UAV and ground nodes (S, U_1, or U_2) is typically characterised by a strong LoS path. In order to deal with LoS and multipath scatterers at the ground receiver, the independent Rician fading is applied to the channel between UAV and ground nodes, whereby the channel coefficients for the links S-R, R-U_1, and R-U_2 being represented by g_{sr}, g_{ru_1}, and g_{ru_2}, respectively. In order to depict the PDF and CDF of the channel gain $|g_{ij}|^2$, for $i \in \{s, r\}$ and $j \in \{r, u_1, u_2\}$, with $i \neq j$, a non-central chi-square distribution with two degrees of freedom is utilised as

$$f_{|g_{ij}|^2}(z) = b_{ij} e^{-K_{ij}} e^{-b_{ij}z} I_0\left(2\sqrt{K_{ij} b_{ij} z}\right)$$
$$= e^{-K_{ij}} e^{-b_{ij}z} \sum_{l=0}^{\infty} \frac{K_{ij}^l b_{ij}^{k+1}}{l! \, \Gamma(l+1)} z^l \quad (5)$$

and

$$F_{|g_{ij}|^2}(z) = 1 - Q\left(\sqrt{2K_{ij}}, \sqrt{2b_{ij} z}\right), \quad (6)$$

where $b_{ij} = (K_{ij} + 1)/\Omega_{ij}$, with $K_{ij} \triangleq |\mu_{ij}|^2/2\sigma^2$, $\Omega_{ij} = d_{ij}^{-\alpha_{ij}}$, $I_0(z)$, and $Q(a, b)$ representing the Rician factor, the normalized average fading power, the first-order modified Bessel function in the zeroth-order, and the Marcum Q-function of the first-order, respectively.

B. PS-Based EH with Source Transmission

In the considered system, an energy harvester is used by the UAV to generate electricity for data transmission and spectrum

sensing. It should be noted that in our study, the energy that is harvested is mostly used for sensing and transmission, while the embedded battery of the UAV is primarily responsible for providing the energy required for UAV flying, hovering, and other expenses. Due to the HD operation employed in the PS-based EH, the block transmission time T is split into two sub-blocks, with one half being utilised for primary transmission (first transmission phase) and the other for secondary transmission (second transmission phase), as illustrated in Fig. 2. Node S transmits a unit-power signal x_s during the first transmission phase, and as a result, the signals received at nodes U_1 and U_2 can be represented by y_{su_1} and y_{su_2}, respectively, and expressed as

$$y_{sj} = h_{sj} \left(\sqrt{P_s}\, x_s + \eta_{ts} \right) + \eta_{rsj} + \Psi_{sj}, \qquad (7)$$

where $j \in \{u_1, u_2\}$, transmit power at S is denoted as P_s, the distortion noise for transmit processing at S is represented by $\eta_{ts} \sim \mathcal{CN}(0, \lambda_{ts}^2 P_s)$, the distortion noise for receive processing at the j-th node is represented by $\eta_{rsj} \sim \mathcal{CN}(0, \lambda_{rsj}^2 P_s |h_{sj}|^2)$, where λ_{ts} and λ_{rsj} represent the severity of the impairments such that $\lambda_{sj} = \sqrt{\lambda_{ts}^2 + \lambda_{rsj}^2}$, and Ψ_{sj} represents the AWGN variable. Consequently, the final SNDR at j-th node, $j \in \{u_1, u_2\}$, via the direct transmission (DT)-link, can be represented as

$$\gamma_{sj}^{\text{DT}} = \frac{\Delta_s\,|h_{sj}|^2}{\Delta_s\,|h_{sj}|^2 \lambda_{sj}^2 + 1}, \qquad (8)$$

where $\Delta_s = \frac{P_s}{\sigma^2}$ be the transmit signal-to-noise ratio (SNR) at node S. The received signal at R is given as

$$y_{sr} = g_{sr} \left(\sqrt{P_s}\, x_s + \eta_{ts} \right) + \eta_{rsr} + \Psi_{sr}, \qquad (9)$$

where $\eta_{rsr} \sim \mathcal{CN}(0, \lambda_{rsr}^2 P_s |g_{sr}|^2)$. Through the use of the PS-based EH parameter ρ ($0 \leq \rho \leq 1$), the R divides the received signal y_{sr} into two parts. In particular, $\sqrt{\rho}\, y_{sr}$ is used to gather energy to refuel its battery, and $\sqrt{1-\rho}\, y_{sr}$ is utilised to analyse information. Consequently, the received signal at the energy harvester's input is provided by

$$\sqrt{\rho}\, y_{sr} = \sqrt{\rho} g_{sr} \left(\sqrt{P_s} x_s + \eta_{ts} \right) + \sqrt{\rho} \eta_{rsr} + \sqrt{\rho} \Psi_{sr}. \quad (10)$$

The energy that R has harvested[2] can be stated using (10) as

$$E_r = \frac{\Theta \rho P_s\, |g_{sr}|^2\, T}{2}, \qquad (11)$$

where $0 \leq \Theta \leq 1$ is the inverter circuitry's energy conversion efficiency at R, and the noise statistic [22] is ignored because we were aiming for harvested energy with $P_r \ll P_s$. The power will be used for the remaining $T/2$ time and will therefore be provided by

$$P_r = \frac{E_r}{T/2} = \Theta \rho P_s\, |g_{sr}|^2 = \beta P_s\, |g_{sr}|^2, \qquad (12)$$

[2]It is worth mentioning hereby that the consideration of a linear EH model, while not fully practical, have a simplification to establish a baseline performance evaluation. Non-linear EH models [6], [20] would be more realistic and shall be undertaken in future works.

where $\beta = \Theta \rho$. Contrarily, the base-band signal that the information receiver (IR) at R has received is represented by

$$\begin{aligned} y_{sr}^{'} &= \sqrt{(1-\rho)} y_{sr} \\ &= \sqrt{1-\rho}\, g_{sr} \left(\sqrt{P_s} x_s + \eta_{ts} \right) + \sqrt{1-\rho}\, \eta_{rsr} \\ &\quad + \sqrt{1-\rho}\, \Psi_{sr} + \Psi_{RF}, \end{aligned} \qquad (13)$$

where Ψ_{RF} denotes the sample AWGN owing to RF to baseband signal conversion. Consequently, the overall AWGN noise at IR is $\Psi_{sr} = \sqrt{1-\rho}\ \Psi_{sr} + \Psi_{RF}$. As a result, the resulting SNDR through the DT-link at node R can be expressed as

$$\gamma_{sr}^{\text{DT}} = \frac{(1-\rho)\Delta_s\,|g_{sr}|^2}{(1-\rho)\Delta_s\,|g_{sr}|^2 \lambda_{sr}^2 + 1}, \qquad (14)$$

where $\lambda_{sr} = \sqrt{\lambda_{ts}^2 + \lambda_{rsr}^2}$.

The DF relaying with OC-NOMA transmission using PS-based EH protocol is described in the next section, and thereby, the users U_1 and U_2's corresponding SINDR expressions are obtained.

C. DF Relaying with OC-NOMA Transmission

Here, R implements a DF-based relaying startegy during the second transmission phase and hence first decodes the primary signal x_s. If R is successful in decoding, it applies the NOMA principle to combine the decoded signal x_s with its own signal x_r to produce a superimposed signal z_r^{DF}. Consequently, the R node's transmit signal is provided by

$$z_r^{\text{DF}} = \sqrt{\delta P_r} x_s + \sqrt{(1-\delta)P_r} x_r + \eta_{tr}. \qquad (15)$$

where the transmit power at R is denoted as P_r, and the distortion noise for transmit processing at R is represented by $\eta_{tr} \sim \mathcal{CN}(0, \lambda_{tr}^2 P_r)$. Following that, the corresponding signals obtained at U_1 and U_2 from R can be represented by $y_{ru_1}^{\text{DF}}$ and $y_{ru_2}^{\text{DF}}$, being provided as

$$y_{rj}^{\text{DF}} = g_{rj}\, z_r^{\text{DF}} + \eta_{rrj} + \Psi_{rj}, \qquad (16)$$

for $j \in \{u_1, u_2\}$. Herein, the distortion noise for receive processing at the j-th node is represented by $\eta_{rrj} \sim \mathcal{CN}(0, \lambda_{rrj}^2 P_r |g_{rj}|^2)$, with λ_{tr} and λ_{rrj} being the severity of the impairments such that $\lambda_{rj} = \sqrt{\lambda_{tr}^2 + \lambda_{rrj}^2}$, and Ψ_{rj} represents the AWGN variable. The SNDR expression at U_1, based on (15) and (16), can be stated as

$$\gamma_{ru_1}^{\text{DF}} = \frac{\delta \beta \Delta_s\, |g_{sr}|^2 |g_{ru_1}|^2}{\beta \Delta_s\, |g_{sr}|^2 |g_{ru_1}|^2 \Xi_p + 1}, \qquad (17)$$

where $\Xi_p = (1-\delta) + \lambda_{ru_1}^2$ with $\lambda_{ru_1} = \sqrt{\lambda_{tu_1}^2 + \lambda_{rru_1}^2}$. The U_1 now exploits MRC to combine the source's signal components received in first transmission phase (via DT) and in second transmission phase, subject to the source's signal being successfully decoded at R (via relay transmission).

The U_2 implements SIC in accordance with the NOMA principle. The U_2 accomplishes this by first decoding the source's signal x_s, removing x_s from $y_{ru_2}^{\text{DF}}$, and then decoding

its own signal x_r. The U_2 first decodes source's signal, while considering the signal R's as noise. In light of (15) and (16), the resulting SINDR expression at U_2 can be stated as

$$\gamma_{ru_2 \to x_s}^{\text{DF}} = \frac{\delta \beta \Delta_s |g_{sr}|^2 |g_{ru_2}|^2}{\beta \Delta_s |g_{sr}|^2 |g_{ru_2}|^2 \Xi_s + 1}, \tag{18}$$

where $\Xi_s = (1 - \delta) + \lambda_{ru_2}^2$ with $\lambda_{ru_2} = \sqrt{\lambda_{tr}^2 + \lambda_{rru_2}^2}$. Remembering that U_2 picks up the source's signal in the first transmission phase, it is now possible for it to use the MRC to decode x_s during the SIC process. U_2 can then decode x_s and take it out of the y_{ru_2} received NOMA signal. When taking into account the iSIC scenario, the SINDR at U_2 can be written as

$$\gamma_{ru_2}^{\text{DF}} = \frac{(1 - \delta) \beta \Delta_s |g_{sr}|^2 |g_{ru_2}|^2}{\beta \Delta_s |g_{sr}|^2 \left(\lambda_{ru_2}^2 |g_{ru_2}|^2 + \delta |h_I|^2 \right) + 1}, \tag{19}$$

where h_I is the residual interference signal (IS) [24] channel coefficient at U_2 and is subject to Nakagami-m fading with fading severity m_I and average power $\mathbb{E}[|h_I|^2] = \xi \Omega_I$. Herein, ξ ($0 \le \xi \le 1$) accounts for the level of residual IS due to iSIC, i.e., $\xi = 0$ implies the case of pSIC.

Again, if decoding of the signal x_s at R in the first transmission phase is unsuccessful, it will not communicate during the second transmission phase. In this scenario, U_1 only receives x_s from the S over the DT-link during the first transmission phase.

III. PERFORMANCE ANALYSIS OF PRIMARY NETWORK

In this part, we analyse the accurate and asymptotic OP performance for the primary network using the PDT and I-CSST schemes. We also look at retrieving the NOMA power allocation parameter's effective value.

A. Accurate OP Analysis

1) PDT Scheme: We now take into consideration that PDT just delivers communication through a DT-link only, with no involvement from UAV-borne relay cooperation. We use this scheme as a benchmark to assess the effectiveness of the suggested I-CSST scheme. The OP of the primary network utilising the PDT scheme for a pre-defined target rate r_{th}^p can be given, by realising that PDT occurs for a single transmission phase, as

$$P_{\text{Pri}}^{\text{DT}}(r_{th}^p) = \Pr \left[\log_2 \left(1 + \gamma_{su_1}^{\text{DT}} \right) < r_{th}^p \right]. \tag{20}$$

Then, (20) can be re-expressed as

$$P_{\text{Pri}}^{\text{DT}}(r_{th}^p) = \Pr \left[\gamma_{su_1}^{\text{DT}} < \tau_p' \right] = F_{\gamma_{su_1}^{\text{DT}}}(\tau_p'), \tag{21}$$

where $\tau_p' = 2^{r_{th}^p} - 1$. The CDF in (21) can be represented using (8) as

$$F_{\gamma_{su_1}^{\text{DT}}}(\tau_p') = \Pr \left[|h_{su_1}|^2 < \frac{\tau_p'}{\Delta_s \left(1 - \lambda_{su_1}^2 \tau_p' \right)} \right], \tag{22}$$

and can be computed, with the condition on threshold τ_p', as

$$F_{\gamma_{su_1}^{\text{DT}}}(\tau_p') = \begin{cases} F_{\gamma_{su_1}} \left(\frac{\tau_p'}{\Delta_s \left(1 - \lambda_{su_1}^2 \tau_p' \right)} \right), & \text{if } \tau_p' < \frac{1}{\lambda_{su_1}^2}, \\ 1, & \text{if } \tau_p' \ge \frac{1}{\lambda_{su_1}^2}. \end{cases} \tag{23}$$

This allows for the computation of the required OP by applying (2) into (23). Note that, starting with (23), PDT induces an outage whenever the threshold τ_p' exceeds the value $\frac{1}{\lambda_{su_1}^2}$.

2) I-CSST Scheme: Now, as described in Section II, we examine the OP performance of the I-CSST scheme for the primary network. The primary network's OP formulation under the I-CSST scheme can be given by considering the target rate r_{th}^p as

$$P_{\text{Pri}}^{\text{CSST}}(r_{th}^p) = \Pr \left[\gamma_{sr}^{\text{DT}} \ge \tau_p, \left(\gamma_{su_1}^{\text{DT}} + \gamma_{ru_1}^{\text{DF}} \right) < \tau_p \right] + \Pr \left[\gamma_{sr}^{\text{DT}} < \tau_p, \gamma_{su_1}^{\text{DT}} < \tau_p \right], \tag{24}$$

where $\tau_p = 2^{2r_{th}^p} - 1$. The OP expression in (24) can be further expressed as

$$P_{\text{Pri}}^{\text{CSST}}(r_{th}^p) = \left(1 - F_{\gamma_{sr}^{\text{DT}}}(\tau_p) \right) \underbrace{\Pr \left[\left(\gamma_{su_1}^{\text{DT}} + \gamma_{ru_1}^{\text{DF}} \right) < \tau_p \right]}_{P_1} + F_{\gamma_{sr}^{\text{DT}}}(\tau_p) F_{\gamma_{su_1}^{\text{DT}}}(\tau_p). \tag{25}$$

We must evaluate the CDF $F_{\gamma_{sr}^{\text{DT}}}(\tau_p)$ and the probability term P_1 in order to calculate (25). Using (14), it is possible to extract the CDF $F_{\gamma_{sr}^{\text{DT}}}(\tau_p)$ as

$$F_{\gamma_{sr}^{\text{DT}}}(\tau_p) = \begin{cases} F_{\gamma_{sr}} \left(\frac{\tau_p}{(1 - \rho) \Delta_s (1 - \lambda_{sr}^2 \tau_p)} \right), & \text{if } \tau_p < \frac{1}{\lambda_{sr}^2}, \\ 1, & \text{if } \tau_p \ge \frac{1}{\lambda_{sr}^2}. \end{cases} \tag{26}$$

Next, P_1 can be evaluated as

$$P_1 = \int_0^{\tau_p} \left(\int_0^{\tau_p - y} f_{\gamma_{ru_1}^{\text{DF}}}(x) \, dx \right) f_{\gamma_{su_1}^{\text{DT}}}(y) \, dy$$
$$= \int_0^{\tau_p} \left(F_{\gamma_{ru_1}^{\text{DF}}}(\tau_p - y) \right) f_{\gamma_{su_1}^{\text{DT}}}(y) \, dy. \tag{27}$$

In order to calculate (27), one needs the CDF $F_{\gamma_{ru_1}^{\text{DF}}}(\cdot)$, which can be determined by using (17) as in the following lemma.

Lemma 1: The Rician fading can be applied to determine the CDF $F_{\gamma_{ru_1}^{\text{DF}}}(w)$ for the I-CSST scheme in the OC-NOMA system as

$$F_{\gamma_{ru_1}^{\text{DF}}}(w) = \begin{cases} \mathbb{A}_1(w) - \mathbb{A}_2(w), & \text{if } w < \frac{\delta}{\Xi_p}, \\ 0, & \text{if } w \ge \frac{\delta}{\Xi_p}, \end{cases} \tag{28}$$

where $\mathbb{A}_1(w)$ and $\mathbb{A}_2(w)$ are, respectively, given as

$$\mathbb{A}_1(w) = \sum_{l=0}^{\infty} \sum_{f=0}^{\infty} \left(\frac{(K_{ru_1})^{l+f}}{(l!)(f!)} \right) e^{-2K_{ru_1}} \tag{29}$$

and

$$\mathbb{A}_2(w) = \sum_{l=0}^{\infty} \sum_{a=0}^{l} \sum_{n=0}^{\infty} \left(\frac{(K_{ru_1})^{l+n} (b_{ru_1})^{a+n+1}}{(l!)(a!)(n!)^2} \right) (T_1)^{\frac{a+n+1}{2}} \times e^{-2K_{ru_1}} \mathcal{K}_{n-a+1} \left(2\sqrt{T_1 b_{ru_1}^2} \right), \tag{30}$$

with $T_1 = \frac{w}{\beta \Delta_s (\delta - \Xi_p w)}$.

Proof: See Appendix A. ∎

Furthermore, by using the expression of $F_{\gamma_{ru_1}^{\text{DF}}}(w)$ from (28) and inserting the PDF expression of $\gamma_{su_1}^{\text{DT}}$ into (27), it is realised that a closed-form solution for P_1 would be intractable. Therefore, we apply an L-stairways conjecture [44] to simplify P_1 as for the complicated integral sector in (27) to obtain

$$P_1 \approx \sum_{n=0}^{L-1} \left\{ F_{\gamma_{su_1}^{\text{DT}}}\left(\frac{n+1}{L}\tau_p\right) - F_{\gamma_{su_1}^{\text{DT}}}\left(\frac{n}{L}\tau_p\right) \right\}$$
$$\times F_{\gamma_{ru_1}^{\text{DF}}}\left(\frac{L-n}{L}\tau_p\right). \tag{31}$$

Finally, $P_{\text{Pri}}^{\text{CSST}}(r_{th}^p)$ can be evaluated by inserting the CDF expressions from (23) and (28) into (31) and the resulting expression together with (23) and (26) into (25).

B. Asymptotic OP Analysis

In order to determine the diversity order, we achieve an asymptotic OP expression in (25) for high SNR ($\Delta_s, \Delta_r \to \infty$). In the beginning, we exploit the fact that the lower incomplete gamma function $\Upsilon(a, z)$ [40, eq. 8.354.1] can be approximated as

$$\Upsilon(a, z) = \sum_{n=0}^{\infty} \frac{(-1)^n z^{a+n}}{n!(a+n)} \underset{z \to 0}{\approx} \left(\frac{z^a}{a}\right). \tag{32}$$

At high SNR, we are able to alter CDF from (2) as

$$F_{|h_{ij}|^2}(z) \approx \frac{1}{\Gamma(m_{ij}+1)} \left(\frac{m_{ij}}{\Omega_{ij}} z\right)^{m_{ij}}. \tag{33}$$

It follows that the PDT scheme's asymptotic OP can be expressed as

$$P_{\text{Pri}}^{\text{DT, asy}}(r_{th}^p) = F_{\gamma_{su_1}^{\text{DT}}}^{\text{asy}}(\tau_p')$$
$$= \frac{1}{\Gamma(m_{su_1}+1)} \left(\frac{m_{su_1} T_2}{\Omega_{su_1}}\right)^{m_{su_1}}, \tag{34}$$

where $T_2 = \frac{\tau_p'}{\Delta_s(1 - \lambda_{su_1}^2 \tau_p')}$. The asymptotic OP for the primary network's I-CSST scheme can be further assessed as

$$P_{\text{Pri}}^{\text{CSST, asy}}(r_{th}^p) = \left(1 - F_{\gamma_{sr}^{\text{DT}}}^{\text{asy}}(\tau_p)\right) \underbrace{\Pr\left[(\gamma_{su_1}^{\text{DT}} + \gamma_{ru_1}^{\text{DF}}) < \tau_p\right]}_{P_1^{\text{asy}}}$$
$$+ F_{\gamma_{sr}^{\text{DT}}}^{\text{asy}}(\tau_p) F_{\gamma_{su_1}^{\text{DT}}}^{\text{asy}}(\tau_p). \tag{35}$$

Asymptotic expressions of the relevant CDFs and the probability term are computed for the evaluation of (35) as follows.

Under Rician fading, the CDF $F_{\gamma_{sr}^{\text{DT}}}^{\text{asy}}(\tau_p)$ for I-CSST system can be stated as

$$F_{\gamma_{sr}^{\text{DT}}}^{\text{asy}}(\tau_p) = \sum_{l=0}^{\infty} \frac{(K_{sr})^l (b_{sr} T_3)^{l+1}}{(l!)^2 (l+1)} e^{-K_{sr}}, \tag{36}$$

where $T_3 = \frac{\tau_p}{(1-\rho)\Delta_s(1-\lambda_{sr}^2 \tau_p)}$ for $\tau_p < \frac{1}{\lambda_{sr}^2}$.

The CDF $F_{\gamma_{ru_1}^{\text{DF}}}^{\text{asy}}(\tau_p)$ can be calculated, similar to condition like (28), as

$$F_{\gamma_{ru_1}^{\text{DF}}}^{\text{asy}}(\tau_p) = \sum_{l=0}^{\infty} \sum_{f=0}^{\infty} \frac{(K_{ru_1} b_{ru_1})^{l+f} (b_{ru_1})^{l-f+2} (T_1)^{(l+1)}}{(l!)^2 (f!)^2 (l+1)}$$
$$\times (f-l-1)! \, e^{(-2K_{ru_1})}, \tag{37}$$

for $\tau_p < \frac{\delta}{\Xi_p}$. Next, P_1^{asy} in (35) can be evaluated, similar to condition (31), as

$$P_1^{\text{asy}} \approx \sum_{n=0}^{L-1} \left\{ F_{\gamma_{su_1}^{\text{DT}}}^{\text{asy}}\left(\frac{n+1}{L}\tau_p\right) - F_{\gamma_{su_1}^{\text{DT}}}^{\text{asy}}\left(\frac{n}{L}\tau_p\right) \right\}$$
$$\times F_{\gamma_{ru_1}^{\text{DF}}}^{\text{asy}}\left(\frac{L-n}{L}\tau_p\right). \tag{38}$$

Finally, $P_{\text{Pri}}^{\text{CSST, asy}}(r_{th}^p)$ can be evaluated by inserting the CDF expressions from (34) and (37) into (38) and the resulting expression together with (34) and (36) into (35). Thus, on applying [45] $d_{\text{Pri}}^{\text{DT}} = -\lim_{\Delta_s \to \infty} \frac{\log(P_{\text{Pri}}^{\text{DT, asy}}(\Delta_s))}{\log(\Delta_s)}$ and $d_{\text{Pri}}^{\text{CSST}} = -\lim_{\Delta_s \to \infty} \frac{\log(P_{\text{Pri}}^{\text{CSST, asy}}(\Delta_s))}{\log(\Delta_s)}$, the primary network's diversity orders for PDT and I-CSST schemes are $d_{\text{Pri}}^{\text{DT}} = m_{su_1}$ and $d_{\text{Pri}}^{\text{CSST}} = m_{su_1} + 1$, respectively.

C. NOMA Power Allocation Parameter

To create the NOMA power allocation policy for R, it is necessary to keep in mind that the QoS criterion for the primary network must be met. To keep the primary network's QoS intact, we actually need to choose an appropriate value for the NOMA power allocation parameter δ. As such, from (28), iterating the conditions $\tau_p < \frac{\delta}{\Xi_p}$, the permissible range of δ for a given threshold τ_p can be calculated as $\frac{\tau_p(1+\lambda_{ru_1}^2)}{1+\tau_p} < \delta < 1$ for the I-CSST scheme. It is worth mentioning that a lower value of δ can allocate more NOMA power for the secondary communication and hence ascertain higher spectrum access possibilities. However, U_1 being a high priority NOMA user, a higher value of δ is allocated correspondingly to U_1.

IV. PERFORMANCE ANALYSIS OF SECONDARY NETWORK

Here, we provide an accurate and asymptotic OP analysis of the secondary network for the I-CSST enabled OC-NOMA system by taking into account the two SIC situations viz., iSIC and pSIC.

A. Accurate OP Analysis

For a target rate of r_{th}^s, the OP formulation for the secondary network under the I-CSST scheme can be expressed as

$$P_{\text{Sec}}^{\text{CSST}}(r_{th}^s) = \Pr[\gamma_{sr}^{\text{DT}} \geq \tau_p]\left(1 - \underbrace{\Pr[\gamma_{u_2}^{\text{MRC}} \geq \tau_p, \gamma_{ru_2}^{\text{DF}} \geq \tau_s]}_{P_2}\right)$$
$$+ \Pr[\gamma_{sr}^{\text{DT}} < \tau_p], \tag{39}$$

where $\tau_s = 2^{r_{th}^s} - 1$. We can evaluate (39) further as

$$P_{\text{Sec}}^{\text{CSST}}(r_{th}^s) = \left[1 - F_{\gamma_{sr}^{\text{DT}}}(\tau_p)\right]\left(1 - P_2\right) + F_{\gamma_{sr}^{\text{DT}}}(\tau_p). \tag{40}$$

The joint probability term P_2 needs to be calculated to evaluate (40). It is deduced in the next subsections for the iSIC and pSIC situations.

1) iSIC: In the subsequent theorem, we derive the expression of P_2 for the instance of iSIC.

Theorem 1: The probability term P_2 in (40) can be calculated under iSIC situation as

$$P_2 = \begin{cases} P_{21} \times P_{22}, & \text{if } \tau_p > \frac{\delta}{\Xi_s}, \\ P_{22}, & \text{if } \tau_p \leq \frac{\delta}{\Xi_s}, \end{cases} \quad (41)$$

with

$$P_{21} \approx 1 - \sum_{n=0}^{L-1} \left\{ F_{\gamma_{su_2}^{\text{DT}}}\left(\frac{n+1}{L}\tau_p\right) - F_{\gamma_{su_2}^{\text{DT}}}\left(\frac{n}{L}\tau_p\right) \right\}$$
$$\times F_{\gamma_{ru_2,x_s}^{\text{DF}}}\left(\frac{L-n}{L}\tau_p\right) \quad (42)$$

and

$$P_{22} = \begin{cases} \mathbb{C}_1(\tau_s) - \mathbb{C}_2(\tau_s), & \text{if } \tau_s < \frac{1-\delta}{\lambda_{ru_2}^2}, \\ 0, & \text{if } \tau_s \geq \frac{1-\delta}{\lambda_{ru_2}^2}, \end{cases} \quad (43)$$

where

$$\mathbb{C}_1(\tau_s) = \sum_{l=0}^{\infty}\sum_{f=0}^{\infty}\sum_{b=0}^{f}\sum_{p=0}^{\infty} \frac{\left(K_{ru_2}^{l+f+p}\right)\left(b_{ru_2}^{b+p+1}\right)}{(l!)(f!)(b!)(p!)^2}(b+p)!$$
$$\times \left(\frac{T_6}{T_5}\right)^b \left(\frac{b_{ru_2}T_6}{T_5} + b_{ru_2}\right)^{-(b+p+1)} e^{-3K_{ru_2}}, \quad (44)$$

and

$$\mathbb{C}_2(\tau_s) = \sum_{l=0}^{\infty}\sum_{a=0}^{l}\sum_{n=0}^{\infty}\sum_{c=0}^{n}\sum_{q=0}^{\infty} \frac{\left(K_{ru_2}^{l+n+q}\right)\left(b_{ru_2}^{a+n+q+2}\right)}{(l!)(a!)(n!)^2(q!)^2}$$
$$\times (n-c+q)!\binom{n}{c}\left(\frac{\tau_s}{T_4}\right)^a \left(\frac{T_6}{T_5}\right)^{n-c}(T_5)^{-(c+1)}$$
$$\times \left(\frac{b_{ru_2}T_6}{T_5} + b_{ru_2}\right)^{-(n-c+q+1)} e^{-3K_{ru_2}}, \quad (45)$$

with $T_4 = \beta\Delta_s$, $T_5 = (1-\delta) - \lambda_{ru_2}^2\tau_s$, and $T_6 = \delta\tau_s$.

Proof: See Appendix B. ∎

The relevant CDFs in (42) can be easily determined similar to (23) and (28). The appropriate OP expression for the secondary network can be obtained by putting the results from (26) and (41) into (40).

2) P-SIC: In this scenario, P_{22} can be used to calculate the OP of the secondary network while using $k_2 = 0$.

$$P_{22} = \begin{cases} \mathbb{D}_1(\tau_s) - \mathbb{D}_2(\tau_s), & \text{if } \tau_s < \frac{1-\delta}{\lambda_{ru_2}^2}, \\ 0, & \text{if } \tau_s \geq \frac{1-\delta}{\lambda_{ru_2}^2}, \end{cases} \quad (46)$$

where

$$\mathbb{D}_1(\tau_s) = \sum_{l=0}^{\infty}\sum_{f=0}^{\infty} \frac{K_{ru_2}^{l+f}}{(l!)(f!)}e^{(-2K_{ru_2})}, \quad (47)$$

$$\mathbb{D}_2(\tau_s) = \sum_{l=0}^{\infty}\sum_{a=0}^{l}\sum_{n=0}^{\infty} \frac{(K_{ru_2})^{l+n}(b_{ru_2})^{a+n+1}}{(l!)(a!)(n!)^2}(T_7)^a e^{(-2K_{ru_2})}, \quad (48)$$

where $T_7 = \frac{\tau_s}{\beta\Delta_s\left[(1-\delta) - \lambda_{ru_2}^2\tau_s\right]}$. Now, on inserting (46) into (41) and the result along with (26) into (40), one can fetch the requisite OP expression.

B. Asymptotic OP Analysis

The secondary network's asymptotic OP can be determined using the formula

$$P_{\text{Sec}}^{\text{CSST, asy}}\left(r_{\text{th}}^s\right) = \left[1 - F_{\gamma_{sr}^{\text{DT}}}^{\text{asy}}(\tau_p)\right]\left(1 - P_2^{\text{asy}}\right) + F_{\gamma_{sr}^{\text{DT}}}^{\text{asy}}(\tau_p). \quad (49)$$

To evaluate (49), we need to obtain the expression of the joint probability term P_2^{asy}. We derive it in the next subsections for the iSIC and pSIC situations.

1) iSIC: For the case of iSIC, we derive the expression of P_2^{asy} as

$$P_2^{\text{asy}} = \begin{cases} P_{21}^{\text{asy}} \times P_{22}^{\text{asy}}, & \text{if } \tau_p > \frac{\delta}{\Xi_s}, \\ P_{22}^{\text{asy}}, & \text{if } \tau_p \leq \frac{\delta}{\Xi_s}, \end{cases} \quad (50)$$

with

$$P_{21}^{\text{asy}} \approx 1 - \sum_{n=0}^{L-1} \left\{ F_{\gamma_{su_2}^{\text{DT}}}^{\text{asy}}\left(\frac{n+1}{L}\tau_p\right) - F_{\gamma_{su_2}^{\text{DT}}}^{\text{asy}}\left(\frac{n}{L}\tau_p\right) \right\}$$
$$\times F_{\gamma_{ru_2,x_s}^{\text{DF}}}^{\text{asy}}\left(\frac{L-n}{L}\tau_p\right) \quad (51)$$

and probability term P_{22}^{asy} in (50) can be evaluated as

$$P_{22}^{\text{asy}} = \sum_{l=0}^{\infty}\sum_{f=0}^{\infty}\sum_{a=0}^{f}\sum_{n=0}^{\infty} \frac{(K_{ru_2})^{l+f+n}(b_{ru_2})^{l+f+n+3}}{(l!)^2(f!)^2(n!)^2(l+1)}e^{(-3K_{ru_2})}$$
$$\times \left(\frac{\tau_s}{T_4}\right)^{l+1}(T_5)^{-(f+1)}(T_6)^{(f-a)}\left(\frac{b_{ru_2}}{T_5}\right)^{-(a-l)}\binom{f}{a}$$
$$\times (a-l-1)!(f-a+n)!\left(\frac{b_{ru_2}T_6}{T_5} + b_{ru_2}\right)^{-(f-a+n+1)}. \quad (52)$$

The relevant CDFs in (51) can be determined similar to (34) and (37). The appropriate OP expression for the secondary network can be obtained by putting the results from (36) and (50) into (49). Hereby, we examine the diversity order $d_{\text{Sec}}^{\text{iSIC}} = -\lim_{\Delta_s \to \infty} \frac{\log(P_{\text{Sec}}^{\text{CSST, asy}}(\Delta_s))}{\log(\Delta_s)}$ to illustrate that $d_{\text{Sec}}^{\text{iSIC}} = 0$. As a result, the corresponding OP curves would attain error floors in the high SNR region.

2) P-SIC: In this scenario, P_{22}^{asy} can be used to calculate the OP of the secondary network while using $k_2 = 0$ as

$$P_{22}^{\text{asy}} = \sum_{l=0}^{\infty}\sum_{f=0}^{\infty} \frac{(K_{ru_2})^{l+f}(b_{ru_2})^{2(l+1)}}{(l!)^2(f!)^2(l+1)}(f-l-1)!$$
$$\times (T_7)^{l+1}e^{(-2K_{ru_2})}. \quad (53)$$

Now, on inserting (53) into (50) and the result along with (36) into (49), one can fetch the requisite OP expression. Hereby, we examine the diversity order $d_{\text{Sec}}^{\text{pSIC}} = -\lim_{\Delta_s \to \infty} \frac{\log(P_{\text{Sec}}^{\text{CSST, asy}}(\Delta_s))}{\log(\Delta_s)}$ to illustrate that $d_{\text{Sec}}^{\text{pSIC}} = 0$. As a result, the corresponding OP curves would attain error floors in the high SNR region.

V. OVERALL OC-NOMA SYSTEM PERFORMANCE

Based on the advancements in earlier parts, we examine the throughput and energy efficiency performance for the entire OC-NOMA system employing I-CSST scheme in this section.

A. System Throughput

For the OC-NOMA system under consideration, the system throughput is a critical performance indicator to evaluate spectrum usage. It indicates the mean spectral efficiency for cooperative communication-based wireless networks [24]. It can be expressed quantitatively as the total of the individual target rates for the primary and secondary communications that can be successfully attained via the Rician and Nakagami-m fading channels for the proposed OC-NOMA system. The deduced OP expressions for both primary and secondary networks allow us to derive the system throughput for the I-CSST scheme as

$$\mathcal{S}_T^{\text{CSST}} = \left[\left(1 - P_{\text{Pri}}^{\text{CSST}} \left(r_{th}^p\right)\right) r_{th}^p + \left(1 - P_{\text{Sec}}^{\text{CSST}} \left(r_{th}^s\right)\right) r_{th}^s \right]. \quad (54)$$

When $r_{th}^p = r_{th}^s = \mathfrak{R}$ is used, the maximum system throughput for the I-CSST scheme is $\mathfrak{R}$, which could be achieved under optimal hardware and pSIC circumstances under a high SNR environment.

B. Energy Efficiency

We can examine the energy efficiency of the EH-based OC-NOMA system under I-CSST scheme by using the throughput equations in (54). Such a study implies that it can assist in designing an EH-aware OC-NOMA system to increase network lifetime. Fundamentally, the system's energy efficiency is defined as the ratio between the amount of provided data and the amount of energy used [24]. As stated in (54), the system throughput for the I-CSST scheme implies the total amount of data provided. In contrast, with the PS-based EH method in the I-CSST scheme, the total energy spent in the system equals the sum of the energy used by the source during the EH phase (which lasts for $T/2$ of time) and its use during the first transmission phase ($T/2$ of time). Notably, the energy used in the second transmission phase is the energy obtained by relay in the EH phase and does not contribute to the system's overall energy consumption. As a result, the energy efficiency for the OC-NOMA system under consideration, using I-CSST scheme, can be represented as

$$\mathcal{E}^{\text{CSST}} = \frac{\mathcal{S}_T^{\text{CSST}}}{\frac{\Delta_s}{2}}, \quad (55)$$

where $\mathcal{S}_T^{\text{CSST}}$ in bps/Hz is given in (54).

VI. DEEP NEURAL NETWORK DESIGN

This section presents the DNN framework for estimating the OP with minimum computational complexity and rapid run time in order to get around the difficulty and time requirements of mathematical analysis and Monte-Carlo simulations. As the calculation of OP depends on various parameters as listed in Table I, we can train a neural network to learn this relationship.
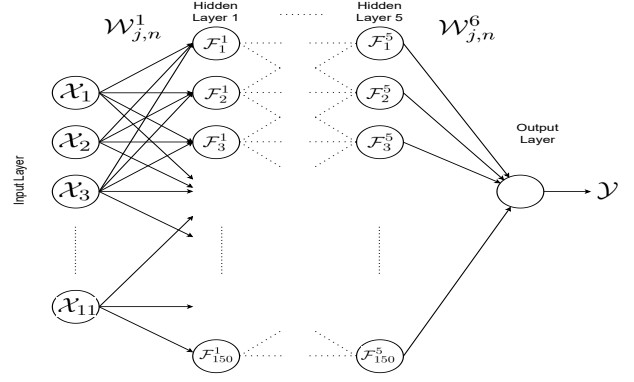

Fig. 3: DNN deployment architecture.

TABLE I: DNN training and testing input parameters.

Parameters (Input)	Values	Parameters (Input)	Values
Δ_s	$[-10, 40]$	λ_0	$[0, 0.3]$
δ	$[0.51, 0.99]$	$r_{\text{th}}^p = r_{\text{th}}^s$	$[0.1, 1]$
Ω_I	$[0, -40]$	r_u	$[0.1, 20]$
$\mathcal{H}_u$	$[0.1, 35]$	φ_u	$[0, 2\pi]$
$(\mathcal{X}_s \mathcal{Y}_s \mathcal{Z}_s)$	$[-20\ 0\ 20]$	$(\mathcal{X}_{u_1} \mathcal{Y}_{u_1} \mathcal{Z}_{u_1})$	$[20{-}20\ 0]$
$(\mathcal{X}_{u_2} \mathcal{Y}_{u_2} \mathcal{Z}_{u_2})$	$[20\ 0\ 0]$	$-$	$-$

A. Dataset Generation Technique

We use a DNN to model the regression problem of predicting the OP for various system conditions. The dataset for this study is constructed using the OP expressions provided in (24) and (39). The calculation of OP depends on various parameters such as SNR (Δ_s), HIs level (λ_0), power factor (δ), target rates ($r_{\text{th}}^p = r_{\text{th}}^s$), level of residual interference (Ω_I), radius of UAV (r_u), height of UAV ($\mathcal{H}_u$), angular motion of UAV (φ_u), locations of source ($\mathcal{X}_s, \mathcal{Y}_s, \mathcal{Z}_s$), location of $U_1(\mathcal{X}_{u_1}, \mathcal{Y}_{u_1}, \mathcal{Z}_{u_1})$, and location of $U_2(\mathcal{X}_{u_2}, \mathcal{Y}_{u_2}, \mathcal{Z}_{u_2})$. Therefore, while constructing the dataset, we should consider different values for each parameter in some defined ranges. The parameters and their ranges are listed in Table I. It is important to note that each system parameter is uniformly sampled in the provided range and later various combinations of these parameters are used with (24) and (39) to generate OP values. Specifically, we picked 5 samples for each parameter.

The resulting dataset $\mathcal{D}$ has a row vector containing dataset $[d] = [\mathcal{X}[d], \mathcal{Y}^{\text{sim}}]$ for each sample d, where $\mathcal{X}[d]$ is a feature vector comprising of all the input variables specified in Table I. Every feature vector $\mathcal{X}[d]$ is utilized to build actual OP sets from (24) and (39), and each one is fed into simulation and given a unique output $\mathcal{Y}^{\text{sim}}$. The total number of samples in the created dataset (D_s) is 10^6, of which 80% are used for training ($D_{s,trn}$), and the remaining 20% are split equally between validation ($D_{s,val}$) and testing ($D_{s,tes}$). We have come to the conclusion that most of the time, this amount of samples is enough to get estimations that are fairly accurate.

Note that with an increase in the number of samples of each parameters in their considered ranges, more data needs to be generated. This is essential for better training of the DNN in order to get high prediction accuracy.

B. DNN Architecture

Our DNN architecture consists of a feed-forward neural network comprising 1 input layer, 5 hidden layers, each containing 150 neurons, and 1 output layer, as depicted in Fig. 3. The eleven parameters given in Section VI-A have corresponding neural counterparts in the eleven input layer neurons. An exponential linear unit (eLU) activation function is used to perform a threshold operation at the output of each neuron in the hidden layers. Any value that is less than zero gets scaled to zero. The eLU is defined mathematically as

$$\text{eLU}(x) = \begin{cases} \varrho\,(e^x - 1), & x < 0, \\ x, & x \geq 0, \end{cases} \quad (56)$$

where x is the input parameter, the constant ϱ has the value 1. Due to its almost linear nature, the eLU activation function has a variety of advantages over the other activation functions. As this is a regression problem to predict the OP value, the output layer of our network contains only one neuron without any subsequent modification or activation function. The output $\mathcal{F}_n^m$ of the n-th neuron in the m-th layer is linked to the outputs of all neurons in the $(m-1)$-th layer and is computed as

$$\mathcal{F}_n^m = \text{eLU}\left(\sum_{j=1}^{\mathcal{U}_{m-1}} \mathcal{W}_{j,n}^m \mathcal{F}_j^{m-1} + \mathcal{C}_n^m \right), \quad (57)$$

where $\mathcal{U}_{m-1}$ is the $(m-1)$-th layer's total number of neurons. $\mathcal{W}_{j,n}^m$ denotes the weight of the link from neuron (j) in layer $(m-1)$ to neuron (n) in layer (m), while $\mathcal{C}_n^m$ denotes the scalar bias in the (m)-th layer.

C. Real-Time Prediction of OP

Training a DNN requires careful optimization of the weights and biases of the network. We employ the Adam optimization algorithm for this purpose. Adam uses a method of gradient descent to update the network's weights and biases during backpropagation. Further, we use the mean squared error (MSE) as the loss function to evaluate the accuracy of the network's predictions, and this value is used to adjust the weights and biases during the optimization process. Let $\mathcal{Y}^d$ and $\bar{\mathcal{Y}}^d$ represent the true and predicted outputs of the DNN for a certain training sample d then the MSE loss of the training phase is calculated as

$$\text{Loss}\big(\mathcal{Y}^d, \bar{\mathcal{Y}}^d\big) = \frac{1}{\mathcal{D}_{s,tes}} \sum_{d=1}^{\mathcal{D}_{s,tes}} \big(\mathcal{Y}^d - \bar{\mathcal{Y}}^d\big)^2. \quad (58)$$

The Adam optimization algorithm is able to adjust the weights and biases of the network to minimize the MSE and improve the accuracy of the predictions generated by the network.

In the following part, we compare the DNN evaluation to mathematical analysis and Monte-Carlo simulation to illustrate how long it takes to execute an OP prediction.

VII. NUMERICAL AND SIMULATION RESULTS

In this section, we perform numerical analysis for the proposed UAV relaying OC-NOMA system and make use of Monte-Carlo simulations in MATLAB version R2022a in

TABLE II: Simulation Parameters [with $j \in \{1, 2\}$].

Parameters	Values
Average fading powers (Ω_{su_j})	0.1, 0.1
Fading severity parameters (m_{su_j})	1, 1
Average power gain of IS channel (Ω_I)	0.1
Rician factor (K)	1
Environment parameters (ε, ξ) [43]	20, 0.5
Uplink and downlink environment (κ, ν)	$-1.5, 3.5$
UAV parameters ($\varphi_u, r_u, \mathcal{H}_u$) [43]	π, 20 m, 35 m
Location of Source ($\mathcal{X}_s, \mathcal{Y}_s, \mathcal{Z}_s$)	$(-20, 0, 20)$ m
Location of U_1 and U_2 ($\mathcal{X}_{u_1}, \mathcal{Y}_{u_1}, \mathcal{Z}_{u_1}$), ($\mathcal{X}_{u_2}, \mathcal{Y}_{u_2}, \mathcal{Z}_{u_2}$)	$(20, -20, 0)$, $(20, 0, 0)$m
Path loss exponent (α_{su_j})	2.2
Level of HIs [46] ($\lambda_{su_j} = \lambda_{sr} = \lambda_{ru_j} = \sqrt{2}\lambda_0$)	$\lambda_0 = 0, 0.3$
PS parameter (ρ)	0.7
Energy conversion efficiency (Θ)	0.75
Block duration (T)	1 sec
Level of stairways conjecture (H)	50
Noise variance (σ^2)	-114 dBm/Hz
Bandwidth (BW)	1 MHz

order to validate our theoretical aspects. Unless otherwise specified, we set up a few system parameters, which are depicted in Table II. While obtaining the path-loss model, $\Omega_{ij} = d_{ij}^{-\alpha_{ij}}$, we utilise a 3-D network configuration. We also set $\lambda_{ts} = \lambda_{tr} = \lambda_{rsu_1} = \lambda_{rsr} = \lambda_{rsu_2} = \lambda_{rru_1} = \lambda_{rru_2} = \lambda_0$ as the level of HIs such that $\lambda_{su_1} = \lambda_{sr} = \lambda_{su_2} = \lambda_{ru_1} = \lambda_{ru_2} = \sqrt{2}\lambda_0$. These parameters are ascertained by the EVMs [46].

A DNN model with five hidden layers and 150 neurons per layer is created using Python 3.7.13 together with Keras 2.8.0 and Tensor-Flow 2.8.0. Throughout the course of 70 training epochs, the DNN's weights are randomly initialised using the Adam optimizer and a gradient decay value of 0.95. It begins with a learning rate of 10^{-3}, which falls to 90% after 20 epochs. All tests are performed on a computer with an i7 − 7700 processor, an 8 GB GeForce GTX 1080 GPU, and 16 GB of RAM. It is important to note that the DNN prediction findings are discovered to be pretty well aligned with the simulation and the analytical results produced from the formulations in Section III-IV for all the subsequent numerical investigations.

Fig. 4 depicts the OP versus source transmit power plots for the primary network, using various target rate values ($r_{th}^p = 0.5$ bps/Hz and $r_{th}^p = 1$ bps/Hz) for both ideal hardware ($\lambda_0 = 0$) and imperfect hardware ($\lambda_0 = 0.3$). In order to fulfill the I-CSST scheme criteria as stated in Section III-C, we select acceptable values of δ. Additionally, for comparison purposes, the OP curves are also produced for the PDT scheme. To start, it is possible to confirm that the simulated and analytical curves are both tightly wedged over the whole power region. In the high power region, the asymptotic curves are also well aligned with the analytical and simulated curves. Additionally, at the fixed target rate, the I-CSST scheme has a substantially lower OP than the PDT scheme. It is noted that all of the curves for the I-CSST scheme (with the specified fading parameters) have a higher slope due to the diversity advantage of using cooperative transmission for the primary network. Although the addition of
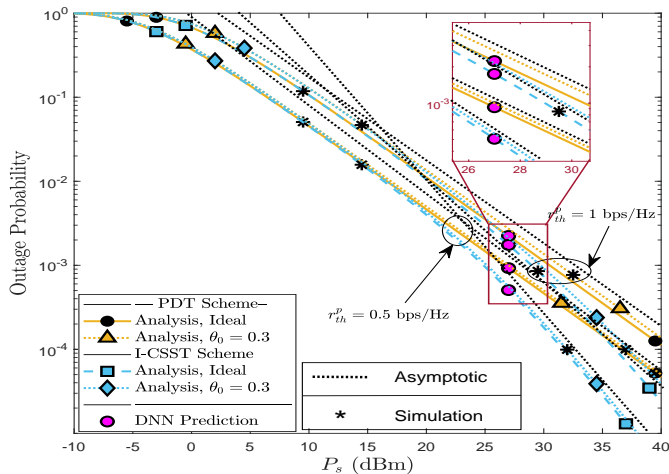
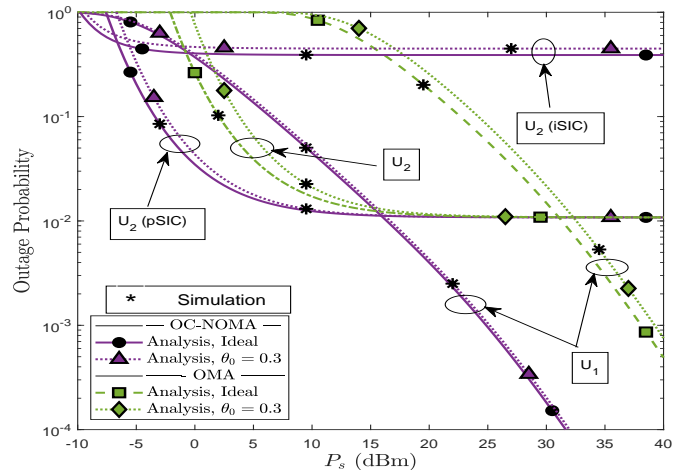Fig. 4: OP performance of the primary network.

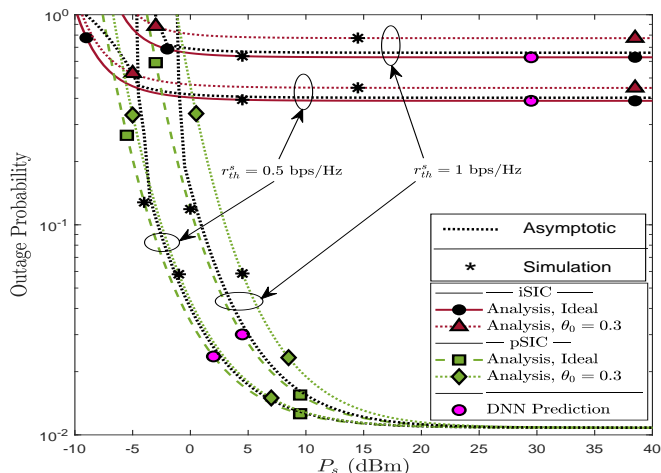Fig. 6: OP performance comparison of NOMA with OMA.
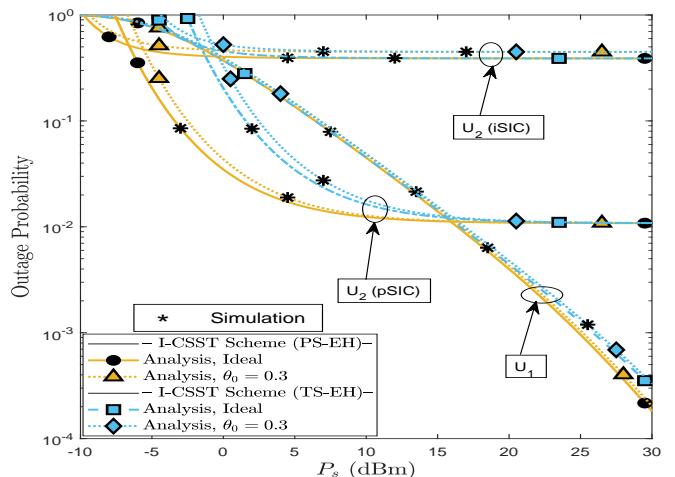

Fig. 5: OP performance of the secondary network.

Fig. 7: OP performance comparison of PS-EH with TS-EH.

HIs ($\lambda_0 = 0.3$) reduces the primary network's performance, its effects are more apparent at higher target rates. Additionally, at the high power regime, the HIs have a stronger impact on the I-CSST scheme. Interestingly, as can be observed, both the DNN prediction and the simulation curves exactly match the analytical calculations given in (21) and (24).

The OP performance of the secondary network in the pSIC and iSIC scenarios is shown in Fig. 5. For this, we set the target rate at $r_{th}^s = 0.5$ bps/Hz and $r_{th}^s = 1$ bps/Hz for both ideal hardware ($\lambda_0 = 0$) and imperfect hardware ($\lambda_0 = 0.3$). To start, it is possible to confirm that the simulated and analytical curves are perfectly aligned throughout the whole power region. In the high power range, the asymptotic curves match the analytical and simulated curves quite well. With I-CSST scheme, the iSIC scenario has a substantially greater OP than the pSIC case. Additionally, for the iSIC situation, an outage floor happens as a result of the IS channel power gain and associated fading severity parameter. The curves resulting from the I-CSST scheme may be seen to stray more from the ideal curve as the level of HIs increases. As evidence of DNN's superior prediction ability, the findings of the DNN

prediction are nearly identical to those of the analytical and simulation results.

The performance comparison between the I-CSST scheme based OC-NOMA and OMA system is shown in Fig. 6. As shown in the plot, U_1 and U_2 (pSIC) case of NOMA outperforms OMA significantly for all power values, whereas U_2 (iSIC) case of NOMA outperforms OMA in regions with low power values. It is because of that, OMA system requires three time slots to run, therefore as a result, the corresponding signal-to-interference-plus-noise ratio (SINR) threshold is higher than its NOMA counterpart. While the imposition of HIs ($\lambda_0 = 0.3$) results in a decline in the OP performance of the I-CSST scheme, its effects on the OMA scheme are more noticeable. As a result, it can be concluded that the I-CSST scheme with NOMA is more resistive to HIs than the OMA counterpart.

Fig. 7 plots the curves for OP against transmit power of the I-CSST scheme with the PS-EH and TS-EH protocols at target rate ($r_{th}^p = 0.5$ bps/Hz) for both ideal hardware ($\lambda_0 = 0$) and imperfect hardware ($\lambda_0 = 0.3$). Firstly, it is confirmed that the simulated and analytical curves closely align throughout the
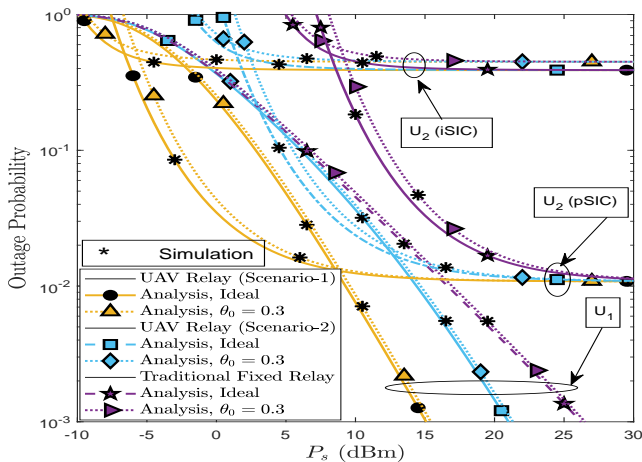
Fig. 8: OP performance comparison of UAV relaying with traditional fixed relaying OC-NOMA system.

Fig. 9: Throughput plots for OC-NOMA system.

Fig. 10: Energy efficiency plots for OC-NOMA system.

entire power range. The plot clearly illustrates that the I-CSST scheme, employing the PS-EH protocol, executes superior outage performance compared to the TS-EH protocol [23]. Specifically, at the high power region, U_1 exhibits improved performance, while at the low power region, U_2 showcases enhanced performance. The inclusion of HIs ($\lambda_0 = 0.3$) results in a degradation in the network's performance. Additionally, in the high power regime, the impact of HIs on the I-CSST scheme becomes more significant for U_1. On the other hand, in the low power regime, the pSIC case for U_2 exhibits performance degradation attributed to HIs.

Fig. 8 illustrates the curves depicting the OP versus transmit power of the OC-NOMA system with UAV relaying and traditional fixed relaying. The target rate is set at $r_{th}^p = 0.5$ bps/Hz. The plot includes results for both ideal hardware conditions ($\lambda_0 = 0$) and imperfect hardware conditions ($\lambda_0 = 0.3$). Specifically, two scenarios are considered for UAV relaying: Scenario-1 ($\varphi_u = \pi, r_u = 20, \mathcal{H}_u = 35$) and Scenario$-2$ ($\varphi_u = \pi, r_u = 11, \mathcal{H}_u = 19$). These scenarios are analyzed to demonstrate the advantages of UAV relaying over the traditional relaying system [21]. Firstly, it is evident that the simulated and analytical curves exhibit a close alignment across the entire power range. As shown in the plot, it is clear that the outage performance of the I-CSST scheme using the UAV relaying system surpasses that of the traditional fixed relaying system. More precisely, in the high power region, U_1 using UAV relaying system demonstrates improved performance, whereas in the low power region, U_2 exhibits enhanced performance. By increasing the radius and height of the UAV, the performance of the system improves significantly. This is because increasing the radius expands the coverage area of the relay, while increasing the height of the UAV enables the relay to cover users at greater distances. Consequently, the combined effect of increased radius and height enhances the overall performance of the system. The inclusion of HIs ($\lambda_0 = 0.3$) results in a degradation in the network's performance.

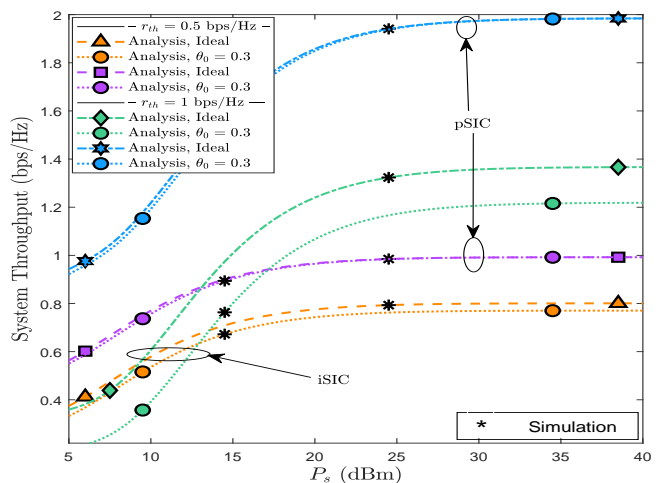In order to get insight into the mean spectral efficiency of
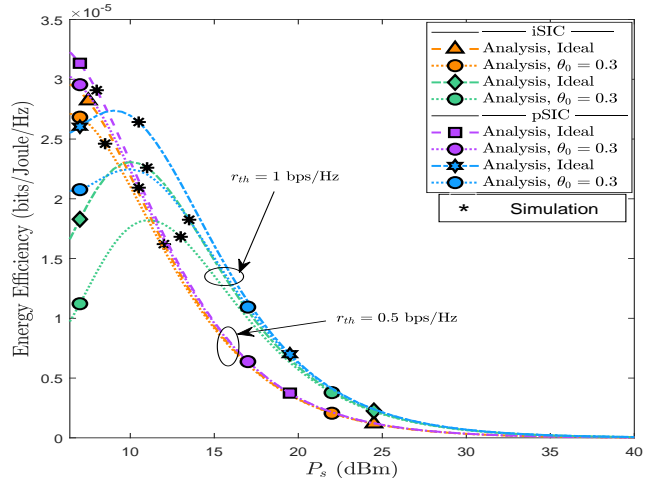
the I-CSST scheme for OC-NOMA system, Fig. 9 highlights the system throughput curves based on the deduced analytical expression in Section V-A. Here, we plot the system throughput versus source transmit power at two different target rates i.e., $r_{th}^p = r_{th}^s = r_{th} = 0.5$ and 1 bps/Hz for both ideal hardware ($\lambda_0 = 0$) and imperfect hardware ($\lambda_0 = 0.3$). The relevant graphs show that, in the low power region, system throughput declines as the target rate increases. In contrast, for the set target rate, the system throughput grows until a specific power value, at which point it becomes saturated. The greatest throughput that can be achieved for the specified target rate is illuminated as this saturated value. This throughput saturation happens significantly at a high power for higher target rate values. This is because outage performance at higher target rates is generally worse than outage performance at lower target rates. Furthermore, it is clear from the two separate HIs values that system throughput declines as HIs levels rise. Additionally, we can also see that the system throughput of the pSIC OC-NOMA system is significantly higher than that of the iSIC OC-NOMA system for the fixed target rate.

Fig. 10 sheds light on the OC-NOMA system's energy effi-

ciency. For two different target rates at $r_{th}^p = r_{th}^s = r_{th} = 0.5$ and 1 bps/Hz under the I-CSST scheme, we draw curves with and without HIs for the system's energy efficiency against source transmit power. The relevant graphs show that as the target rate is raised, the system's energy efficiency decreases at mid power values. It is clear from looking at two distinct levels of HIs ($\lambda_0 = 0, 0.3$) that, in contrast to the ideal scenario, HIs cause a drop in the system's energy efficiency. This demonstrates that the performance of energy efficiency suffers when HIs are imposed. Additionally, it is clear from the pertinent curves that the system achieves optimal energy efficiency at a specific power value for a given target rate and levels of HIs. The power value at which the system operates at its most energy-efficient level likewise fluctuates when the desired rate and levels of HIs change. It is important to note that when the power value rises, the energy efficiency of the system under consideration falls. The main cause of this is increased power consumption compared to system throughput at higher power.

Above all, the execution times of the DNN assessment, mathematical analysis, and Monte Carlo simulation for the suggested system are compared. The results demonstrate that the DNN prediction approach needs just 0.0227 seconds to produce OP values. The mathematical evaluation takes 0.0519 seconds, however the Monte Carlo simulation took 7.1965 seconds to produce the OP values.

VIII. CONCLUSION

We evaluated the effectiveness of an OC-NOMA system using EH-based I-CSST scheme while considering the effects of practically created iSIC and HIs at the transceiver nodes. In particular, we adopted Rician and Nakagami-m fading channels to quantify the total OC-NOMA system performance in terms of OP of primary and secondary networks, system throughput, and energy efficiency. Additionally, we provide some guidance on selecting the NOMA power allocation factor's value for effective spectrum sharing. It is demonstrated that I-CSST scheme outperforms the benchmark PDT scheme. Above all, the I-CSST scheme with NOMA is shown to outperform OMA for the high data rate requirements. Our theoretical results in this paper help in providing the design guidelines for ameliorating spectral efficiency and energy efficiency in future wireless networks. According to numerical findings, the outputs of the DNN prediction for OP tightly matched the outcomes of the Monte-Carlo simulation and analysis. In light of this, using a DNN as a black box could be a new, promising, and efficient way for assessing system performance using a low-latency estimation procedure that does not require the formulation of challenging complicated equations in actual network scenarios.

APPENDIX A

The CDF $F_{\gamma_{ru_1}^{\text{DF}}}(w) = \Pr\left[\gamma_{ru_1}^{\text{DF}} < w\right]$ is expressed, using (17), as

$$F_{\gamma_{ru_1}^{\text{DF}}}(w) = \Pr\left[\frac{\delta\beta\Delta_s |g_{sr}|^2 |g_{ru_1}|^2}{\beta\Delta_s |g_{sr}|^2 |g_{ru_1}|^2 \Xi_p + 1} < w\right]$$
$$= \Pr\left[|g_{sr}|^2 < \frac{w}{\beta\Delta_s(\delta - \Xi_p w)|g_{ru_1}|^2}\right], \quad (59)$$

which can be further simplified as

$$F_{\gamma_{ru_1}^{\text{DF}}}(w) = \int_0^\infty \left(\int_0^{T_1 y^{-1}} f_{|g_{sr}|^2}(x)dx\right) f_{|g_{ru_1}|^2}(y)dy. \quad (60)$$

On substituting the expression of PDFs using (5) and solving using [40, eq. 1.111], one can reach at the desired result in (28).

APPENDIX B

Now taking $P_2 = \Pr\left[\tau_p - \gamma_{ru_2,x_s}^{\text{DF}} \leq \gamma_{su_2}^{\text{DT}}, \tau_s \leq \gamma_{ru_2}^{\text{DF}}\right]$, inserting the appropriate SNDR expressions from (8), (18), and (19) and retrieving the $|h_{ru_2}|^2$ condition to get the expression in (41), we can perform an analysis for $\tau_p < \gamma_{ru_2,x_s}^{\text{DF}}$ and $\tau_p > \gamma_{ru_2,x_s}^{\text{DF}}$. The term $P_{21} = 1 - \Pr\left[\gamma_{su_2}^{\text{DT}} < \tau_p - \gamma_{ru_2,x_s}^{\text{DF}}\right]$ can be evaluated in this case utilising the L-stairways conjecture to get the result in (42). In contrast, the $P_{22} = \Pr\left[\gamma_{ru_2}^{\text{DF}} \geq \tau_s\right] = 1 - F_{\gamma_{ru_2}^{\text{DF}}}(x)$ can be assessed for $T_5 > 0$ as

$$P_{22} = 1 - \int_0^\infty \int_{\frac{T_6 z}{T_5}}^\infty \int_0^{\frac{\tau_s}{T_4(T_5 y - T_6 z)}} f_{|g_{sr}|^2}(x) f_{|g_{ru_2}|^2}(y) \times f_{|h_I|^2}(z) \, dxdydz. \quad (61)$$

On substituting the expression of PDF $f_{|g_{sr}|^2}(x)$ and solving the inner integral using [40, eq. 3.351.1], (61) can be simplified as $P_{22} = \int_0^\infty \left(\mathbb{B}_1(\tau_s) - \mathbb{B}_2(\tau_s)\right) f_{|h_I|^2}(z) \, dz$, where

$$\mathbb{B}_1(\tau_s) = \int_{\frac{T_6 z}{T_5}}^\infty \sum_{l=0}^\infty \frac{K_{ru_2}^l}{(l!)} e^{-K_{ru_2}} f_{|g_{ru_2}|^2}(y)dy \quad (62)$$

and

$$\mathbb{B}_2(\tau_s) = \int_{\frac{T_6 z}{T_5}}^\infty \sum_{l=0}^\infty \sum_{a=0}^l \frac{K_{ru_2}^l b_{ru_2}^a}{(l!)(a!)} \left(\frac{\tau_s}{T_4}\right)^a e^{-K_{ru_2}} f_{|g_{ru_2}|^2}(y)dy. \quad (63)$$

Thus, on invoking the expression of PDFs $f_{|g_{ru_2}|^2}(y)$ and $f_{|h_I|^2}(z)$, and solving the associated integral with the help of [40, eq. 3.351.2] and [40, eq. 3.351.3], we obtain P_{22} as presented in (43).

REFERENCES

[1] G. Gui, M. Liu, F. Tang, N. Kato, and F. Adachi, "6G: Opening new horizons for integration of comfort, security, and intelligence," *IEEE Wireless Commun.*, vol. 27, no. 5, pp. 126-132, Oct. 2020.
[2] M. B. Pandian, M. L. Sichitiu, and H. Dai, "Optimal resource allocation in random access cooperative cognitive radio networks," *IEEE Trans. Mobile Comp.*, vol. 14, no. 6, pp. 1245-1258, Jun. 2015.
[3] F. Shan, J. Luo, W. Wu, M. Li, and X. Shen, "Discrete rate scheduling for packets with individual deadlines in energy harvesting systems," *IEEE J. Sel. Areas Commun.*, vol. 33, no. 3, pp. 438-451, Mar. 2015.

[4] D. Gao, L. Wang, and B. Hu, "Spectrum efficient communication for heterogeneous IoT networks," *IEEE Trans. Netw. Sci. Eng.*, vol. 9, no. 6, pp. 3945-3955, Nov.-Dec. 2022.

[5] T. Wu and H. -C. Yang, "RF energy harvesting with cooperative beam selection for wireless sensors," in *Proc. IEEE Wireless Commun. Lett.*, vol. 3, no. 6, pp. 585-588, Dec. 2014.

[6] H. -V. Tran and G. Kaddoum, "Robust design of AC computing-enabled receiver architecture for SWIPT networks," *IEEE Wireless Commun. Lett.*, vol. 8, no. 3, pp. 801-804, Jun. 2019.

[7] M. Bouabdellah *et al.*, "Cooperative energy harvesting cognitive radio networks with spectrum sharing and security constraints," *IEEE Access*, vol. 7, pp. 173329-173343, Nov. 2019.

[8] R. C. Qiu *et al.*, "Cognitive radio network for the smart grid: Experimental system architecture, control algorithms, security, and microgrid testbed," *IEEE Trans. Smart Grid.*, vol. 2, no. 4, pp. 724-740, Dec. 2011.

[9] S. Thakur and A. Singh, "Secrecy performance of underlay cognitive radio networks with primary interference," *IEEE Trans. Netw. Sci. Eng.*, vol. 9, no. 4, pp. 2641-2657, 1 Jul.-Aug. 2022.

[10] D. K. Verma, R. Y. Chang, and F. -T. Chien "Energy-assisted decode-and-forward for energy harvesting cooperative cognitive networks," *IEEE Trans. Cogn. Commun. and Netw.*, vol. 3, no. 3, pp. 328-342, Sep. 2017.

[11] J. He, S. Guo, G. Pan, Y. Yang, and D. Liu, "Relay cooperation and outage analysis in cognitive radio networks with energy harvesting," *IEEE Syst. Journ.*, vol. 12, no. 3, pp. 2129-2140, Sep. 2018.

[12] Z. Ding *et al.*, "A survey on non-orthogonal multiple access for 5G networks: Research challenges and future trends," *IEEE J. Sel. Areas Commun.*, vol. 35, no. 10, pp. 2181-2195, Oct. 2017.

[13] Y. Liu, Z. Ding, M. Elkashlan, and J. Yuan, "Non-orthogonal multiple access in large-scale underlay cognitive radio networks," *IEEE Trans. Veh. Technol.*, vol. 65, no. 12, pp. 10152-10157, Dec. 2016.

[14] L. Lv, J. Chen, Q. Ni, Z. Ding, and H. Jiang, "Cognitive non-orthogonal multiple access with cooperative relaying: A new wireless frontier for 5G spectrum sharing," *IEEE Commun. Mag.*, vol. 56, no. 4, pp. 188-195, Apr. 2018.

[15] S. Arzykulov, G. Nauryzbayev, T. A. Tsiftsis, B. Maham, and M. Abdallah, "On the outage of underlay CR-NOMA networks with detect-and-forward relaying," *IEEE Trans. Cogn. Commun. Netw.*, vol. 5, no. 3, pp. 795-804, Sep. 2019.

[16] L. Lv, Q. Ni, Z. Ding, and J. Chen, "Application of non-orthogonal multiple access in cooperative spectrum-sharing networks over Nakagami-*m* fading channels," *IEEE Trans. Veh. Technol.*, vol. 66, no. 6 , pp. 5510-5515, Jun. 2017.

[17] X. Zhang *et al.*, "Outage performance of NOMA-based cognitive hybrid satellite-terrestrial overlay networks by amplify-and-forward protocols," *IEEE Access*, vol. 7, pp. 85372-85381, Jun. 2019.

[18] V. Singh, P. K. Upadhyay, and M. Lin, "On the performance of NOMA-assisted overlay multiuser cognitive satellite-terrestrial networks," *IEEE Wireless Commun. Lett.*, vol. 9, no. 5, pp. 638-642, May 2020.

[19] Y. Xu *et al.*, "Joint beamforming and power-splitting control in downlink cooperative SWIPT NOMA systems," *IEEE Trans. Signal Process.*, vol. 65, no. 18, pp. 4874-4886, Sep. 2017.

[20] D. Wang and S. Men, "Secure energy efficiency for NOMA based cognitive radio networks with nonlinear energy harvesting," *IEEE Access*, vol. 6, pp. 62707–62716, Oct. 2018.

[21] T. -H. Vu and S. Kim, "Performance evaluation of power-beacon-assisted wireless-powered NOMA IoT-based systems," *IEEE Internet Things J.*, vol. 8, no. 14, pp. 11655-11665, Jul. 2021.

[22] A. K. Shukla, J. Sharanya, K. Yadav, and P. K. Upadhyay, "Exploiting SWIPT-enabled IoT-based cognitive nonorthogonal multiple access with coordinated direct and relay transmission," *IEEE Sensor J.*, vol. 22, no. 19, pp. 18988-18999, Oct. 2022

[23] Y. Yu, Z. Yang, Y. Wu, J. A. Hussein, W. -K. Jia, and Z. Dong, "Outage performance of NOMA in cooperative cognitive radio networks with SWIPT," *IEEE Access*, vol. 7, pp. 117308-117317, Sep. 2019.

[24] C. K. Singh and P. K. Upadhyay, "Overlay cognitive IoT-based full-duplex relaying NOMA systems with hardware imperfections," *IEEE Internet Things J.*, vol. 9, no. 9, pp. 6578-6596, May 2022.

[25] H. Huang *et al.*, "Deep learning for physical-layer 5G wireless techniques: Opportunities, challenges and solutions," *IEEE Wireless Commun.*, vol. 27, no. 1, pp. 214-222, Feb. 2020.

[26] T. -H. Vu, T. -V. Nguyen, and S. Kim, "Wireless powered cognitive NOMA-based IoT relay networks: Performance analysis and deep learning evaluation," *IEEE Internet Things J.*, vol. 9, no. 5, pp. 3913-3929, Mar. 2022.

[27] Z. Zhang, Y. Lu, Y. Huang, and P. Zhang, "Neural network-based relay selection in two-way SWIPT-enabled cognitive radio networks," *IEEE Trans. Veh. Technol.*, vol. 69, no. 6, pp. 6264-6274, Jun. 2020.

[28] G. Gui, H. Huang, Y. Song, and H. Sari, "Deep learning for an effective non-orthogonal multiple access scheme," *IEEE Trans. Veh. Technol.*, vol. 67, no. 9, pp. 8440-8450, Sep. 2018.

[29] G. Manogaran, T. N. Nguyen, J. Gao, and P. M. Kumar, "Deep learning-based service distribution model for wireless network assisted internet of everything," *IEEE Trans. Netw. Sci. Eng.*, vol. 9, no. 5, pp. 3004-3014, Sep.-Oct. 2022.

[30] X. Li, J. Li, Y. Liu, Z. Ding, and A. Nallanathan, "Residual transceiver hardware impairments on cooperative NOMA networks," *IEEE Trans. Wireless Commun.*, vol. 19, no. 1, pp. 680-695, Jan. 2020.

[31] C. K. Singh, V. Singh, P. K. Upadhyay, and M. Lin, "Energy harvesting in overlay cognitive NOMA systems with hardware impairments," *IEEE Syst. Journ.*, vol. 16, no. 2, pp. 2648-2659, Jun. 2022.

[32] E. Bjornson, P. Zetterberg, M. Bengtsson, and B. Ottersten, "Capacity limits and multiplexing gains of MIMO channels with transceiver impairments," *IEEE Commun. Lett.*, vol. 17, no. 1, pp. 91-94, Jan. 2013.

[33] V. Singh, S. Solanki, P. K. Upadhyay, D. B, da Costa, and J. M. Moualeu, "Performance analysis of hardware-impaired overlay cognitive satellite–terrestrial networks with adaptive relaying protocol," *IEEE Syst. Journ.*, vol. 1, no. 15, pp. 192-203, Mar. 2021.

[34] G. Im and J. H. Lee, "Outage probability for cooperative NOMA systems with imperfect SIC in cognitive radio networks," *IEEE Commun. Lett.*, vol. 23, no. 4, pp. 692-695, Apr. 2019.

[35] D. -T. Do, A. -T. Le, and B. M. Lee, "NOMA in cooperative underlay cognitive radio networks under imperfect SIC," *IEEE Access*, vol. 68, no. 8, pp. 4709-4722, Aug. 2020.

[36] S. Arzykulov *et al.*, "Hardware- and interference-limited cognitive IoT relaying NOMA networks with imperfect SIC over generalized non-homogeneous fading channels," *IEEE Access*, vol. 8, pp. 72942-72956, Apr. 2020.

[37] S. Ghosh, A. Al-Dweik, and M. -S. Alouini, "On the performance of end-to-end cooperative NOMA-based IoT networks with wireless energy harvesting," *IEEE Internet Things J.*, doi: 10.1109/JIOT.2023.3267564, Apr. 2023.

[38] S. Jeong, O. Simeone, and J. Kang, "Mobile edge computing via a UAV mounted cloudlet: Optimization of bit allocation and path planning," *IEEE Trans. Veh. Technol.*, vol. 67, no. 3, pp. 2049–2063, Mar. 2018.

[39] M. Dai, Y. Wu, L. Qian, Z. Su, B. Lin, and N. Chen, "UAV-assisted multi-access computation offloading via hybrid NOMA and FDMA in marine networks," *IEEE Trans. Netw. Sci. Eng.*, vol. 10, no. 1, pp. 113-127, Jan.-Feb. 2023.

[40] I. S. Gradshteyn and I. M. Ryzhik, *Tables of Integrals, Series and Products*, 6th ed. New York: Academic Press, 2000.

[41] J. Mu, R. Zhang, Y. Cui, N. Gao, and X. Jing, "UAV meets integrated sensing and communication: Challenges and future directions," *IEEE Commun. Mag.*, vol. 61, no. 5, pp. 62-67, May 2023.

[42] H. Yan, S. -H. Yang, Y. Chen, and S. A. Fahmy, "Optimum battery weight for maximizing available energy in UAV-enabled wireless communications," *IEEE Wireless Commun. Lett.*, vol. 10, no. 7, pp. 1410-1413, Jul. 2021.

[43] S. Solanki, J. Park, and I. Lee, "On the performance of IRS-aided UAV networks with NOMA," *IEEE Trans. Veh. Technol.*, vol. 71, no. 8, pp. 9038-9043, Aug. 2022.

[44] C. Zhang, J. Ge, J. Li, Y. Rui, and M. Guizani, "A unified approach for calculating outage performance of two-way AF relaying over fading channels," *IEEE Trans. Veh. Technol.*, vol. 64, no. 3, pp. 1218-1229, Mar. 2015.

[45] X. Yue, Y. Liu, S. Kang, A. Nallanathan, and Z. Ding, "Exploiting full/half-duplex user relaying in NOMA systems," *IEEE Trans. Commun.*, vol. 66, no. 2, pp. 560-575, Feb. 2018.

[46] *8 Hints for making and interpreting EVM measurements*, Tech. Rep., Agilent Technologies, Santa Clara, CA, USA, 2005.